

# Lattice Gas Model for the Drying-Mediated Self-Assembly of Nanorods

Claudia G. Sztrum-Vartash and Eran Rabani\*

School of Chemistry, The Sackler Faculty of Exact Sciences, Tel Aviv University, Tel Aviv 69978, Israel

Received: February 21, 2010; Revised Manuscript Received: May 8, 2010

A coarse-grained lattice gas model is developed to study drying-mediated self-assembly of nanorods. Out-of-equilibrium simulations of the model provide insight into the dynamics of solvent evaporation and the formation of ordered arrays of nanorods. Two different initial depositions of the nanorods on the substrate are studied: a random deposition and a prealigned deposition. We show that an initial random alignment of the nanorods in a thin liquid layer typical of drop casting experiments leads to local order only on time scales relevant for experiments. On the other hand, long-range order can be achieved when external forces are used to prealign the nanorods before evaporation. The effects of nanorod coverage, aspect ratio, spatial and orientational diffusion, and evaporation schemes are discussed.

## I. Introduction

Colloidal prepared nanoparticles are expected to take a major role in the present revolution of nanoscience and nanotechnology. This is due to the fact that it is possible to control their properties arising from the quantum confinement effect<sup>1</sup> by simply changing their size.<sup>2,3</sup> Early studies have focused on the development of synthetic procedures that provide control over the size distribution of the nanoparticles<sup>4</sup> and the assembly of these building blocks into well-defined ordered arrays.<sup>5</sup> Currently, many different assembly schemes exist for *spherical* nanoparticles leading to fascinating superstructures that are governed by various influences, such as the interactions,<sup>6–13</sup> the drying kinetics and coarsening mechanisms,<sup>14–25</sup> hydrodynamic effects,<sup>26–28</sup> and the diffusion of particles and domains.<sup>29,30</sup>

More recently, the focus has shifted to the development of novel fabrication techniques for various *shapes*, such as nanorods,<sup>31–35</sup> tetrapods,<sup>31,36,37</sup> hollow nanoparticles,<sup>38</sup> and nanoparticle heterostructures.<sup>39–44</sup> The opportunity to tune the *shape* of the nanoparticles opens novel directions in device applications such as fluorescence tags for biological imaging,<sup>45,46</sup> optical gain media,<sup>47,48</sup> electronic devices,<sup>49</sup> thermoresponsive materials,<sup>50</sup> and solar cells.<sup>51,52</sup>

A key factor in the fabrication of these devices lies in the ability to develop viable self-assembly schemes with bottom-up approaches.<sup>53,54</sup> Indeed, a significant effort has been devoted to study the assembly of these building blocks, and in particular of nanorods, into well-defined ordered arrays.<sup>55–62</sup> In this respect, nanorods are rather challenging since their anisotropy leads to different types of oriented assemblies, often characterized by short-ranged order, a shortcoming of current assembly schemes. Recent studies have pointed out the difficulty in implementing assembly techniques suitable for spherical particles<sup>16</sup> to nanorods and tetrapods.<sup>59</sup> This has led to the application of external forces to align the nanorods, such as electric<sup>63–68</sup> or magnetic fields.<sup>69</sup>

Despite significant progress made in the control of the self-assembly of nanorods, at this point, our understanding of the process is quite limited. In the current study we examine the evaporation induced self-assembly of nanorods from the theoretical perspective. Recent computer simulation studies have focused on the phase diagram of hard rods with different aspect

ratios.<sup>70–72</sup> Here, we focus on understanding the relevant time scales (the interplay between rotational motion, translation motion, and evaporation dynamics) and length scales (role of the nanorod aspect ratio) on the assembly into ordered arrays. Our approach is based on a coarse-grained model and includes the description of the nanorods as well as that of the solvent on length scales that are equal or larger than the typical correlation length of bulk liquid. Small length scale fluctuations, which are typically Gaussian, will be integrated out.<sup>73</sup> In Section II we provide the details of our model and discuss technical issues related to the simulations. The challenge here is to describe the translational and rotational motion of the nanorods along with the solvent fluctuations on time scales (minutes) and length scales (micrometers) that are relevant for experiments. The importance of solvent fluctuations has been discussed in our previous work for self-assembly of spherical nanoparticles, where heterogeneous evaporation and vapor hole nucleation require explicit treatment of solvent fluctuations beyond the mean field limit.<sup>16–21</sup> Our approach is motivated by the recent developments of lattice gas models due to Chandler and co-workers.<sup>73,74</sup>

In Section III we provide a comprehensive study of the model using Monte Carlo (MC) simulation techniques. We cover a wide range of model parameters, including the role of nanorod coverage, aspect ratio, spatial and orientational diffusion, and evaporation schemes. We wish to address the question whether it is possible and under which conditions one can obtain long-range order structures in the evaporation induced self-assembly scheme. Thus, we focus on two different initial conditions that mimic different experimental realizations: a random deposition and a prealigned deposition. We show that an initial random alignment of the nanorods in a thin liquid layer leads to local order only on time scales that can be probed experimentally. On the other hand, long-range order is achieved when a mechanism of prealignment is included. Finally, in Section V we conclude.

## II. Model

The description of the self-assembly process for nanorods cannot be complete without considering the *translational* and *rotational* motion of the nanorods along with the description of solvent fluctuations and evaporation on time scales relevant

\* To whom correspondence should be addressed.

for experiments.<sup>55,58,59,64</sup> Thus, the approach we developed to describe the self-assembly of spherical nanoparticles,<sup>16,17,21</sup> where the rotational motion and angular dependence can be ignored, calls for a major revision.

One possible route to describe the drying-mediated assembly of nanorods is based on continuous models used successfully, for example, in the description of the self-assembly of fluid membranes.<sup>75</sup> This type of coarse-grained models includes the solvent in a mean field way, but ignores explicitly its fluctuations, which for the present application is crucial. On the other hand, lattice models such as those developed for the self-assembly spherical nanoparticles offer simplicity but limit the motion of the nanoparticles to the lattice directions. In this section we present an approach that, on one hand, is simple enough to describe both the nanorods and the solvent in the relevant length and time scales and also allows for the description of a more complex motion of these building blocks. In many ways, the approach we present is a computational marriage between a continuous model and a lattice model, and thus may also be applicable to other systems, including those mentioned for biological applications.

To allow for the translational and rotational motion of our building blocks and to remain within the advantageous simplicity of the lattice description, we include two layers of grids: an outer layer which is similar to that used to describe the spherical nanoparticle<sup>16</sup> but can account for partial occupancy and an inner layer that is used to describe the motion and interactions. The outer layer keeps the physical dimensions, i.e., the units of length and energy, and provides a platform for graphical representations. The motion of the nanorods and the solvent is described at the inner layer with physical constraints determined by the outer lattice.

For the outer layer, we divide the space into cells, where each cell can contain nanorods, liquid, or gas.<sup>16</sup> The size of each cell in the outer layer equals the typical solvent correlation length,  $\xi$ . The density of each species is described by a variable that can take values *between* 0 (low density) and 1 (high density). This is in contrast to the case developed for spherical nanoparticles, where each variable can take a value of *either* 0 or 1. As will become clear below, the actual value of each variable at the outer level is determined by the occupancy of this cell as represented by the inner layer. However, a single lattice site is bound by total density of all species (liquid, gas, and nanorods) that is 1. We label the density of the solvent and nanorods at a lattice site  $o$  ( $o$  for outer) as  $l_o$  and  $r_o$ , respectively.

The description of the orientational direction of the nanorods on the outer level is quite difficult, unless cells at the outer level can be occupied partially such that at different orientations the liquid–nanorod and air–nanorod surface tensions and the chemical potential are approximately preserved (within a fraction of  $k_B T$ ). This is to prevent artifacts where nanorods align along a preferred direction on the square lattice and also to exclude evaporation of the solvent as a result of nanorod rotations. In other words, the energetics of the system need not depend on the direction of the lattice with respect to the orientation of the nanorods. To describe partial occupancy of each cell in the outer layer we divide it into smaller cells. This forms an inner layer of a denser grid. We label the density of the solvent and nanorods at an inner lattice site  $i$  ( $i$  for inner) as  $l_i$  and  $r_i$ , respectively where each variable can be *either* 0 (if it is not occupied by the species) or 1 (if it is occupied by the species).

In Figure 1 we show typical configurations of a single nanorod on the outer layer and also how an inner layer is formed by the division procedure. As can be seen clearly in the figure, cells

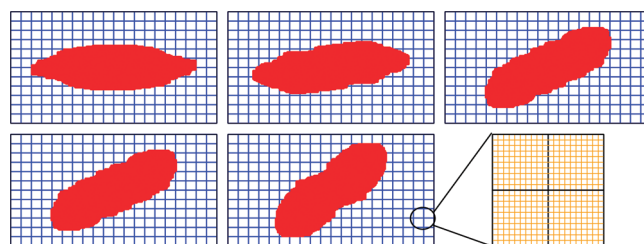


**Figure 1.** Configurations generated for five different angles by the Monte Carlo procedure for a  $16\xi \times 4\xi$  nanorod.

in the outer layer can be partially occupied. The ratio between the number of cells in the inner layer to the number of cells in the outer layer,  $N_o$ , is a parameter determined by converging the result of the relevant observables. In the applications reported below the typical value is  $N_o \approx 100$ . The total density of the liquid at an outer site  $o$  is given by  $l_o = (1/N_o)\sum_{i \in o} l_i$  and similarly for the nanorod  $r_o = (1/N_o)\sum_{i \in o} r_i$ .

The energetics of the system is determined by the following lattice gas model Hamiltonian:

$$H = -\epsilon_l \sum_{\{ij\}} l_i l_j - \epsilon_r \sum_{\{ij\}} r_i r_j - \epsilon_{rl} \sum_{\{ij\}} r_i l_j - \mu \sum_i l_i \quad (1)$$

where the indexes  $i$  and  $j$  belong to the inner layer. The strength of liquid–liquid, nanorod–nanorod, and nanorod–liquid interactions is given by  $\epsilon_l$ ,  $\epsilon_r$ , and  $\epsilon_{rl}$ , respectively. Our model also includes a chemical potential,  $\mu$ , that is used to establish the average concentration of liquid and vapor cells at equilibrium. A large negative value of  $\mu$  will favor evaporation, while positive values will favor wetting. The sums in the above Hamiltonian denoted by  $\{ij\}$  include interactions between cells that are separated by the length of the outer layer  $\xi$  (in contrast to previous models that include only one layer where interactions are taken to be nearest neighbors). In the limit where cells in the outer layer can take the values of 0 or 1, the present scheme of calculating the interactions reduces to the conventional nearest neighbors model. However, when cells are partially occupied it allows for a consistent description of the physical length and energy scales despite the introduction of a denser grid, which has no physical relevance.

As pointed out above, the introduction of two layers is required so that the nanorods do not have preferred orientation on the square lattice in the presence and absence of solvent. To achieve this we have developed the following scheme: We discretize the angles of the nanorod such that they can assume discrete values with an angle spacing defined by  $\Delta\theta$ , for example every  $\Delta\theta = 10$  deg; i.e., we generate nanorod configurations at angles 0,  $\Delta\theta$ ,  $2\Delta\theta$ , etc. To allow an unbiased rotational diffusion of nanorods at infinite dilution in the presence and absence of solvent one has to preserve for each angle the nanorod surface tension and its volume. This is done by a MC procedure where the shape of the nanorod for each angle is slightly modified (within the limits of one outer cell) with the following constraints: the symmetry of inversion must be conserved; the energy as given by eq 1 of the system for all angles must equal within a small fraction of  $k_B T$ ; the energy of a pair of nanorods at different angles must be equal within a small fraction of  $k_B T$  (in the numerical results shown below this fraction is smaller than 10% of  $k_B T$ ); and the aspect ratio of the nanorods at different angles must be preserved.

To fulfill these requirements we perform a MC procedure such that the shape of the nanorod on the denser grid is slightly

modified by choosing two lattice sites that are related by an inversion symmetry operation and reversing their lattice values simultaneously to achieve the desired shape and energy. Such moves are accepted with Metropolis criteria with a Boltzmann probability that is determined by the difference in energy between a given angle and the average energy over all angles. If the algorithm does not converge we increase the value of  $N_o$  until solutions are found. The outcome of such a procedure is depicted in Figure 1, where five configurations of a  $16\xi \times 4\xi$  rod are shown. The remaining angles are obtained by mirror symmetry. The final outcome can be rough on the length scale of the inner grid but, as can be seen in Figure 1, is smooth on the physical length scale  $\xi$  of the outer grid.

Once the configurations of the nanorods are prepared we simulate the dynamics of the self-assembly utilizing a stochastic process for the fluctuations of the solvent density and for nanorods spatial and rotational diffusion. We start from a random or ordered configuration of nanorods at a desired coverage, as depicted by the relevant experimental situation. The remaining cells that are not occupied by the nanorods are filled with solvent. We evolved the configurations by MC dynamics similar to the propagation scheme of spherical nanoparticles.<sup>16,17,21</sup> The variables associated with the nanorods ( $r_o$ ) conserve the corresponding density (conserved order parameter), while the variables representing the solvent ( $l_o$ ) do not conserve density (nonconserved order parameter).<sup>76</sup>

For each MC step we attempt to convert a randomly chosen lattice cell  $o$  of the outer layer that is not occupied by a nanorod from liquid to vapor (or vice versa), and accept such a move with a Metropolis probability with the Hamiltonian specified by eq 1. Cells that are partially filled/empty (as a result of the partial filling of cell due to the nanorods) are also considered. If such cells are filled with solvent then we try to empty them and vice versa if they are empty. The nanorods perform a random walk on the lattice, biased by their interactions with their surroundings. For simplicity we assume that the diffusion constants of an isolated nanorod along the longitudinal and transverse directions are equal (in the hydrodynamic limit they differ by approximately a factor of 2). Specifically, we attempt to displace a nanorod in a random direction with a step chosen from  $\Delta r = [0...1]\xi$  ( $\xi$  is a random number between 0 and 1) and to perform a rotation in an arbitrary direction by changing the angle of the nanorod by the discrete angular spacing. Such a move is accepted with the same Metropolis probability, but only if the region into which the nanorod moves is completely filled with solvent. Solvent density in lattice cells overtaken by this displacement is regenerated into cells that were “released” by the nanorod. This final constraint mimics the very low mobility of the nanoparticles on dry surfaces.<sup>29</sup> It also provides an additional coupling between the kinetics of evaporation and nanorod phase separation.

Control over the relative rates of evaporation compared with the translation and rotational diffusion is achieved by performing  $N_{\text{trans}}$  and  $N_{\text{rot}}$  translation and rotational steps, respectively, for each evaporation move. A full MC step includes an attempt to convert all liquid/vapor cells and to perform  $N_{\text{trans}}$  translation moves and  $N_{\text{rot}}$  rotational moves for all nanorods.

### III. Simulations of Drop-Casting

The simulations reported in this section correspond to an experimental setup where a drop of solvent containing the nanorods is placed on a substrate and the system favors evaporation. Thus, to mimic such experimental conditions we assume that the nanorods are initially distributed randomly in

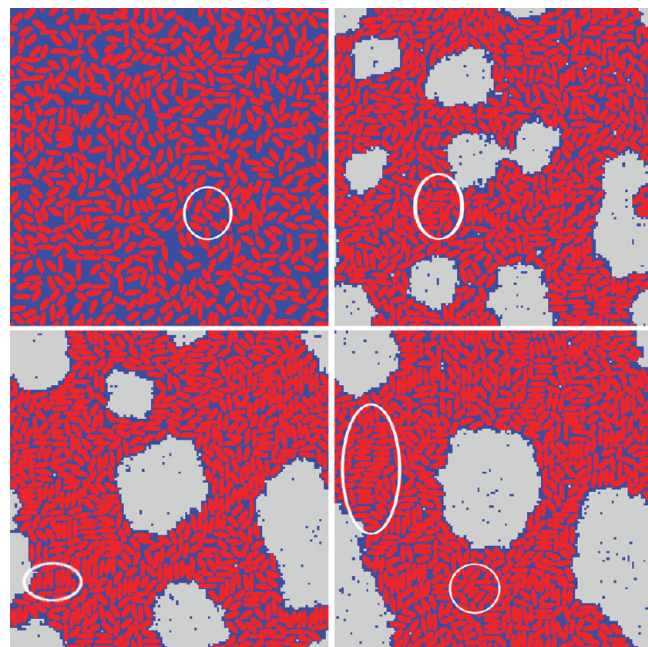


**Figure 2.** Snapshots for typical trajectories for nanorods  $8\xi \times 2\xi$  with total coverage of 50% under homogeneous evaporation conditions. Time increases from upper left to lower right ( $t = 0, 50, 400$ , and  $1600$  in units of  $\tau_1$ ). Examples for oriented clusters are marked with white circles.

the simulation box with the remaining cells filled with the solvent. Furthermore, we fix the chemical potential  $\mu$  and the temperature  $T$  to values for which the system will favor evaporation. During the runs we fix the coverage of the nanorods, the evaporation rate is fixed by the value of the chemical potential, and the diffusivity of the nanorods is fixed by the choice of spatial and angular moves. The parameters that are common to all the simulation results reported below are  $\epsilon_r = \epsilon_l = \epsilon_v$  in units of  $\epsilon_i$ . These parameters are chosen to ensure that the interactions between nanorods are screened by the solvent such that self-organization of nanorods occurs only when the solvent evaporates.<sup>10–12</sup> We will consider two limits of evaporation dynamics corresponding to the homogeneous and heterogeneous cases, as discussed by us for spherical nanoparticles.<sup>16</sup> We also examine the effect of the nanorods size and aspect ratio on the simulated morphologies and describe the role of nanorod spatial and orientational diffusivity. Unless otherwise noted, we use  $\xi$  as the measure of length and the evaporation time  $\tau_1$  as the measure of time.

**A. Homogeneous Evaporation.** In Figure 2 we plot snapshots from simulated trajectories under homogeneous evaporation, at early, intermediate, and late times, for small nanorods  $8\xi \times 2\xi$ . The total coverage is  $\sim 50\%$ , the chemical potential is  $\mu = -2^{1/2}\epsilon_1$ , and the temperature is fixed at  $T = 1/2\epsilon_1$ . Red, blue, and gray represent the nanorods, liquid, and vapor, respectively. This color scheme is kept throughout the paper. Initially the nanorods are distributed randomly in the simulation box with a fixed orientation and the remaining cells are filled with liquid. We propagate this initial configuration for several thousands of MC steps until equilibrium is reached keeping the density of the solvent fixed. The final morphology of this equilibration run is shown in the upper left panel of Figure 2 and serves as the initial configuration for the drying-mediated assembly. As can be seen clearly the angular distribution of the nanorods is random and also the density is relatively uniform. Occasionally, we observe aligned clusters of nanorods even before the solvent has evaporated. These clusters form and break dynamically on

time scales associated with the translational and rotational diffusion hindered by the dense packing. Clustering before evaporation was also observed when we turned off the attractions between the nanorods as long as the concentration of nanorods is high enough. Therefore, the local alignment of nanorods before evaporation is a result of nanorod density fluctuations and may even persist for relatively long times due to the sluggish motion of the nanorods at dense packing conditions.

Next, we propagate this equilibrated initial configuration where we allow for evaporation of the solvent. Similar to the case of spherical nanoparticles, under these conditions, the evaporation of the solvent simply triggers the self-organization into dense and sparse domain, reminiscent of spinodal decomposition of liquid–gas separation. Domains continue to grow after the solvent has nearly disappeared since the interface of the nanorod domains remains wet and fluxional throughout the growth process. The size of the domains is mainly determined by the spatial and angular diffusion of the nanorods, as analyzed below.

At intermediate times ( $t \approx 50\tau_l$ , upper right panel) after the solvent has evaporated, the system self-organizes into a ribbon-like structure. As the time progresses the system anneals slowly toward equilibrium by a similar mechanism reported for spherical nanoparticles.<sup>16,18</sup> During this process the vapor–nanorod and nanorod–nanorod interfacial energy reduces gradually and the nanorods pack into a denser superstructure as can be seen in the lower right panel of Figure 2, where a morphology corresponding to the longest time simulated is shown ( $t \approx 1600\tau_l$  or 16384 MC steps). Similar morphologies have been observed experimentally for many different materials.<sup>55–62</sup> The fact that the present model describes this picture qualitatively (and perhaps also quantitatively) is indicative of the inclusion of the important physical factors in the model. Note that at the longest time simulated here we observe only short-range orientational order of nanorods. Several domains with the longest local orientational order are highlighted in the figure.

To quantify the range of alignment we define a distribution of oriented cluster size  $P_C(n)$ , where  $n \geq 2$  is the number of nanorods in a cluster (bundle) with the same orientation  $\pm\Delta\theta$  degrees at closest packing.  $P_C(n)$  is obtained by associating adjacent nanorods with the same orientation  $\pm\Delta\theta$  to a cluster and then averaging the result for each cluster size  $n$  at a given time  $t$  over many simulation runs. In Figure 3 we plot  $P_C(n)$  at different simulation times for  $\sim 30\%$  (left panels) and  $\sim 50\%$  (right panels) nanorod coverage for different ratios of translational to rotational diffusive moves. Common to all cases shown is the increase of  $P_C(n)$  with time for large oriented clusters. This is mostly correlated with low coverage and with larger spatial and rotational diffusivity. However, for time scales accessible by the simulations (similar to those studied experimentally), the largest oriented bundles observed are relatively short ranged (not exceeding  $n < 15$ ).

The role of the density on the range of alignment is expected, since high packing hinders mainly the rotational motion of the nanorods and thus at higher densities the nanorods follow the air–solvent contact line until their orientation is fixed when the solvent disappears. The effect of translational and rotational diffusivity is somewhat less obvious. When we increase the rotational diffusion rate as compared to the translational diffusion rate the distribution of oriented nanorod clusters approaches the long time limit quite rapidly. On the other hand, when the translational diffusivity is larger than the rotational one,  $P_C(n)$  resembles the case of low diffusivity at early times

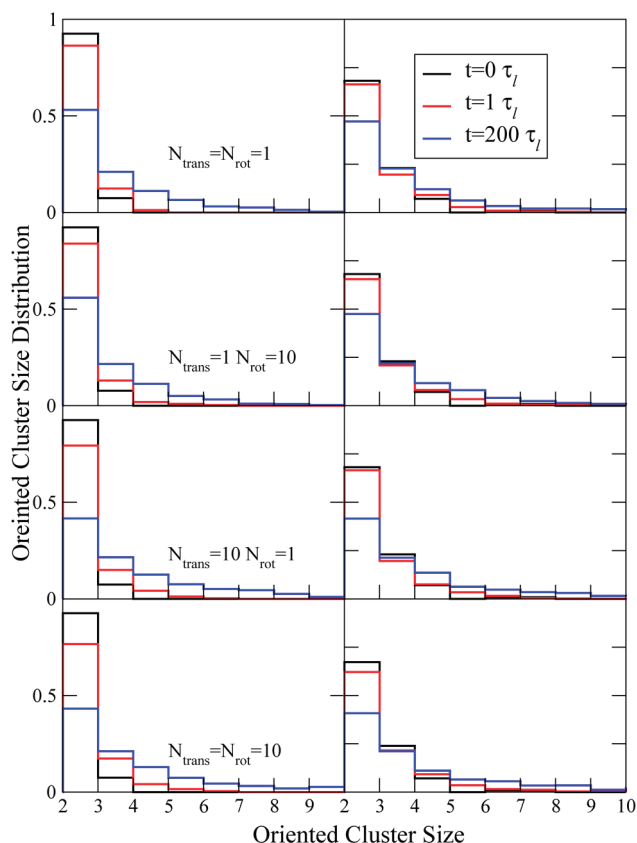


**Figure 3.** Oriented cluster size distribution,  $P_C(n)$ , for  $8\xi \times 2\xi$  nanorods for low coverage (30%, left panels) and high coverage (50%, right panels) at different times.

and of large rotational diffusivity at long times. The overall probability of observing larger oriented clusters is slight larger when the spatial motion overtakes rotational motion. This implies that small oriented bundles grow more rapidly when spatial fluctuations dominate. In other words, formation of large oriented clusters is correlated mainly with rapid translational motion of the nanorods rather than their rotational motion. This is consistent with the mechanism by which oriented clusters grow, which requires local fluctuations in the density of nanorods, fluctuations that are naturally more correlated with spatial motion that lead to larger voids for reorientation to take place.

We note in passing that the diffusion coefficients of an infinitely dilute solution of nanorods depend on the nanorods length and diameter. Ignoring end-effects, the rotational and translational diffusion coefficients are approximated by:<sup>77,78</sup>

$$D_{\text{rot}} = \frac{3k_B T \ln(L/D)}{\pi \eta L^3} \quad (2)$$

$$D_{\text{trans}} = \frac{k_B T \ln(L/D)}{3\pi \eta L}$$

where  $k_B$  is the Boltzmann constant,  $T$  is the temperature,  $L$  and  $D$  are the nanorod length and diameter, and  $\eta$  is the viscosity of the solvent. The ratio between rotational and translation diffusion constants is thus given by:

$$\frac{D_{\text{rot}}}{D_{\text{trans}}} = \frac{9}{L^2} \quad (3)$$

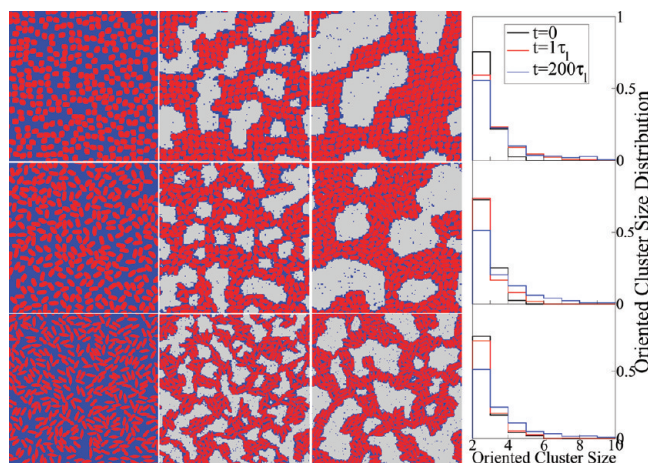


**Figure 4.** Snapshots from typical trajectories for total coverage of 50% under homogeneous evaporation conditions; upper, middle and lower panels correspond to nanorods of size  $6\xi \times 4\xi$ ,  $10\xi \times 4\xi$ , and  $16\xi \times 4\xi$ , respectively. Time increases from left to right ( $t = 0, 50, 1600$  in units of  $\tau_1$ ). Right panels show the oriented cluster size distribution for the corresponding nanorod trajectories at different times. The results at  $t > 200\tau_1$  are practically similar to the result for  $t = 200\tau_1$ , and thus are not shown here.

independent of the diameter of the rod. For the nanorods considered in this work, a ratio of  $N_{\text{trans}}/N_{\text{rot}} \approx 10-30$  is consistent with the continuum hydrodynamic theory. Hence, the more realistic case shown in Figure 3 is that where  $N_{\text{rot}} = 1$  and  $N_{\text{trans}} = 10$ .

To better understand the effect of the size, we have conducted simulations on a variety of nanorods of different size and aspect ratio. In Figure 4 we plot typical snapshots of trajectories for three different nanorods, for total coverage of  $\sim 50\%$ ,  $\mu = -2^{1/2}\epsilon_1$  and  $T = 1/\epsilon_1$ . Upper, middle, and lower panels correspond to nanorods with an aspect ratio of  $1^{1/2}$  ( $6\xi \times 4\xi$ ),  $2^{1/2}$  ( $10\xi \times 4\xi$ ), and  $4$  ( $16\xi \times 4\xi$ ), respectively. The evolution of these systems is qualitatively similar to the case described earlier for nanorods of size  $8\xi \times 2\xi$ , and is not repeated here. One major notable difference is associated with the size of nanorod domains, which for a given time decreases with increasing nanorod dimensions/aspect ratios. In Figure 5 we show the average domain size as a function of time for a series of nanorods of identical diameter. For spherical nanoparticles, following a transient period, the growth of domains under homogeneous evaporation conditions is self-similar with an average size that scales as  $R \propto t^\alpha$  with  $\alpha = 1/3$ , as is often the case in phase separation.<sup>79</sup> In this respect, the present model reproduces the result for spherical nanoparticles previously reported by us.<sup>16</sup> As the aspect ratio of the nanorods increases the transient period before reaching the  $R \propto t^{1/3}$  regime is considerably stretched. In fact, for nanorods with an aspect ratio above  $5/2$ , the time scale accessible by simulations is too short to observe this crossover. The growth of domain is still given by the same power law, but with  $\alpha$  that depends strongly on the aspect ratio of nanorods, decreasing from about  $1/3$  in spherical nanoparticles to  $1/20$  for nanorods with an aspect ratio of 4. The slowing down of the growth of nanorod domains is expected; however, it is quite surprising how promptly coarsening becomes sluggish and how suddenly  $\alpha$  decreases with the nanorod aspect ratio. The dramatical change in the time scales for coarsening provides an explanation as to why assembly of nanorods by drying kinetics is not efficient.

Similarly, we find that the order within dense nanorod domains also depends strongly on the aspect ratio and the

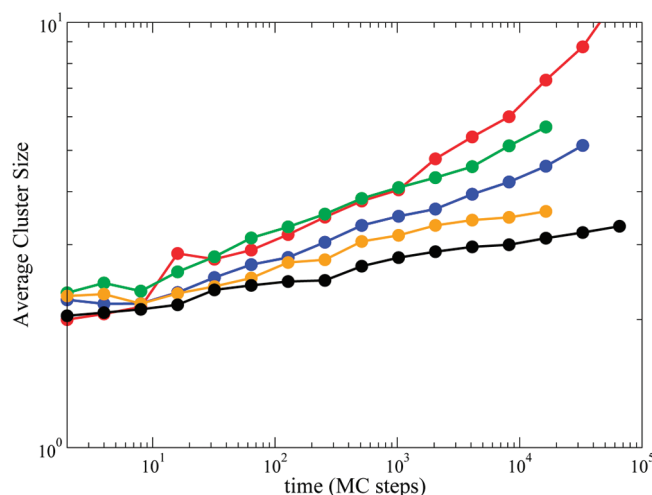


**Figure 5.** Average cluster size as a function of time on a logarithmic scale for nanorods of size  $4\xi \times 4\xi$  (red),  $6\xi \times 4\xi$  (green),  $8\xi \times 4\xi$  (blue),  $10\xi \times 4\xi$  (orange), and  $16\xi \times 4\xi$  (black). The long time behavior can be fit to a scaling law  $R \propto t^\alpha$ , with  $\alpha = 0.29, 0.16, 0.13, 0.044$ , and  $0.042$ , in increasing aspect ratio order.

dimensions of the nanorods. In this respect, nanorods with small aspect ratio ( $1^{1/2}$ ) behave in much the same way as spherical nanoparticles. The orientational order, if it exists, is very short ranged, as clearly can be seen in the corresponding right-hand panel where we plot the oriented cluster size distribution. In this case, the maximal cluster size does not exceed  $n_{\text{max}} = 4$  members. In fact,  $P_C(n)$  is very close to the limit of random orientational packing given by (for  $\Delta\theta < \pi/3$ ):

$$P_C^{\text{rnd}}(n) = \frac{\pi - 3\Delta\theta}{3\Delta\theta} \left(\frac{3\Delta\theta}{\pi}\right)^{n-1} h(n-2) \quad (4)$$

where  $\Delta\theta$  is the angle discretization spacing and  $h(x)$  is the Heaviside step function. On the other hand, nanorods with higher aspect ratio assemble into structures with local orientational order. As before, the range of order is relatively short and is mainly limited by the hindered rotational motion of nanorods at high packing. On the time scales of the simulations, the thermodynamic limit<sup>70-72</sup> is thus not recovered.

Further analysis of the correlation between the range of orientational order and the nanorod aspect ratio is shown in the left panel of Figure 6, where we plot the average oriented cluster size ( $\langle n \rangle = \sum_n n P_C(n)$ ) as a function of the aspect ratio at different times. Under homogeneous evaporation conditions we find that the orientational order increases with time and with aspect ratio; however, it is difficult to define a universal rule for the dependence of  $\langle n \rangle$  on both parameters. Moreover, even for a given aspect ratio (the case corresponding to  $16\xi \times 4\xi$  and  $8\xi \times 2\xi$ ),  $\langle n \rangle$  can be quite different. This can be understood by close examination of the morphologies resulting from the drying kinetics for these two nanorod sizes. As is evident from the snapshots (not shown), the growth kinetics of domains is faster for smaller nanorods. This is a result of the fact that smaller nanorods allow for more solvent to be trapped between them due to the smaller surface area and the weaker nanorod–nanorod attractions. The trapped solvent provides the necessary room for the nanorods to reorient leading to more rapid growth of domains and clusters with longer orientational correlations.

In the left panel of Figure 6 we have scaled the time with  $\tau_1$ . A similar picture emerges when the time of the simulations was scaled with either the spatial diffusion time,  $\tau_{\text{trans}} = \xi^2/D_{\text{trans}}$ , or

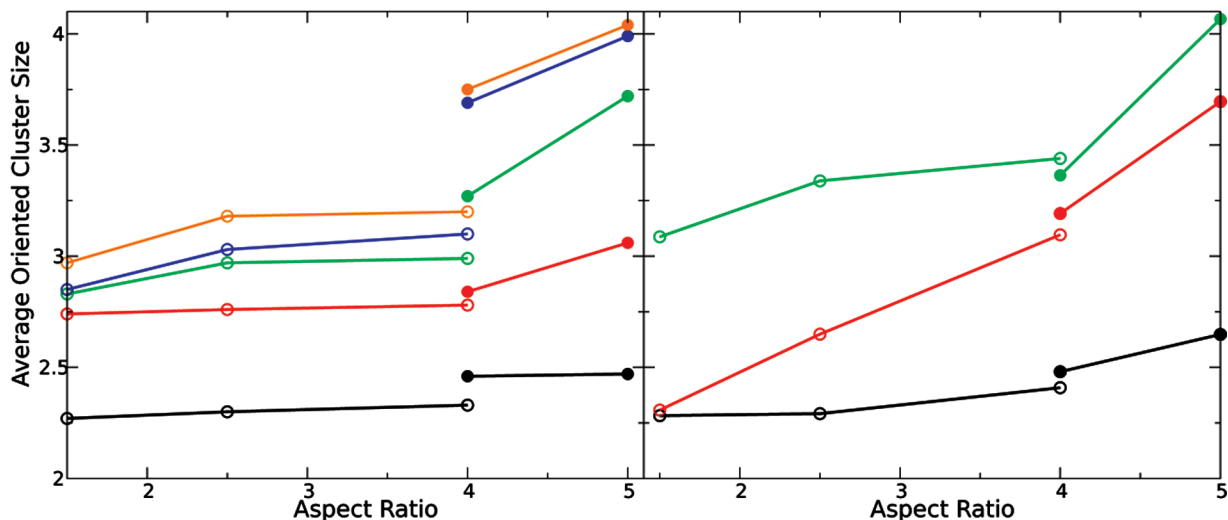


**Figure 6.** Average oriented cluster size ( $\langle n \rangle = \sum_n n P_C(n)$ ) as a function of the nanorods aspect ratio. Filled circles represent nanorods with diameter  $2\xi$  and hollow circles represent nanorods with diameter  $4\xi$ . Left panel: Black, red, green, blue, and orange symbols correspond to  $t = 0, 10, 50, 100$ , and  $200$  in units of  $\tau_1$ , respectively. Right panel: Black, red, and green symbols correspond to average domain size of  $R \approx 5\xi$ ,  $R \approx 30\xi$ , and  $R \approx 40\xi$ .

**TABLE 1: Translation and Rotational Diffusion Constants for  $N_{\text{trans}} = 10$  and  $N_{\text{rot}} = 1$  at 50% Coverage<sup>a</sup>**

	$6 \times 4$	$8 \times 4$	$10 \times 4$	$16 \times 4$	$8 \times 2$
$D_{\text{trans}}$	1.085	1.055	1.05	0.9	0.8
$D_{\text{rot}}$	0.01	0.0083	0.0083	0.0036	0.0046

<sup>a</sup>  $\xi$  and  $\tau_1$  are the units of length and time, respectively.

with the rotational diffusion time,  $\tau_{\text{rot}} = 1/D_{\text{rot}}$ . In Table 1 we summarize the diffusion coefficients at 50% coverage. The translations diffusion constant is roughly the same for all systems considered while the rotational diffusion constant spans a fraction of a decade ( $1/3$  of a decade). Compared with the infinitely diluted system, there is a pronounced effect of packing mainly on the rotational motion, where the rotational diffusion constant can decrease by an order of magnitude ( $D_{\text{rot}} = 0.03$  at infinite dilution) compared with the translational diffusion constant that reduces by a factor of 2 only ( $D_{\text{trans}} = 1.8$  at infinite dilution). The results summarized in Table 1 can be used to explain why scaling the time by other means rather than  $\tau_1$  leads to a similar qualitative picture shown in Figure 6.

The above results suggest that perhaps scaling the time by the average cluster size ( $R \sim t^a$ ) would provide means for understanding the dependence of  $\langle n \rangle$  on the aspect ratio. In the right panel of Figure 6 we plot  $\langle n \rangle$  as a function of the aspect ratio of the nanorods where time was scaled such that each point corresponds to a similar average domain size of the nanorods (similar length scale). Scaling the time in this way leads to a linear relation between the average oriented cluster size and the aspect ratio. More importantly, as can be seen clearly, nanorods with the same aspect ratio ( $16\xi \times 4\xi$  and  $8\xi \times 2\xi$ ) display similar average oriented cluster size at early, intermediate, and late times, suggesting that the proposed scaling is universal.

**B. Heterogeneous Evaporation.** When evaporation is instead heterogeneous in space (rather than homogeneous) the dynamics of self-assembly can be dramatically different.<sup>16,19</sup> In this case evaporation occurs by nucleation and growth of vapor bubbles. This limit of evaporation dynamics has been explored by us for spherical nanoparticles for a single component system<sup>16,19</sup> and for binary mixtures.<sup>18</sup> Under heterogeneous evaporation conditions spherical nanoparticles form network structures where the shapes of terminal structures are determined

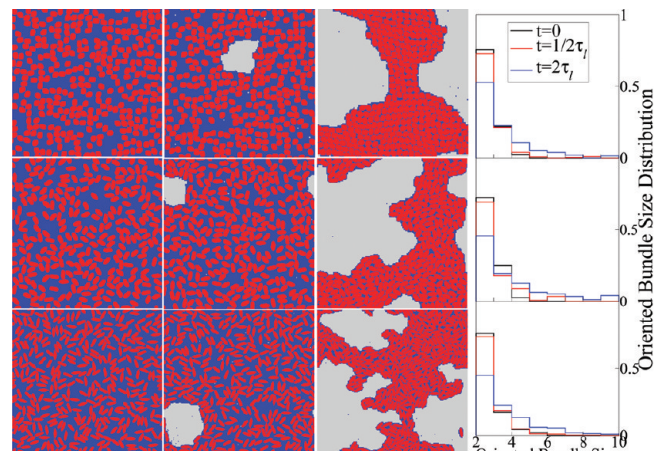


**Figure 7.** Snapshots of typical trajectories for total coverage of 50% under heterogeneous evaporation conditions; upper, middle, and lower panels correspond to nanorods of size  $6\xi \times 4\xi$ ,  $10\xi \times 4\xi$ , and  $16\xi \times 4\xi$ , respectively. Time increases from left to right  $t = 0, 1/2, 6$  in units of  $\tau_1$ . Right panels show the oriented cluster size distribution for the corresponding nanorod trajectories at different times. The results at  $t = 2$  and  $6$  are identical under the current set of model parameters.

primarily by the relative time scales of evaporation and nanoparticle motion. If the nanoparticles are sufficiently mobile to track the fronts of growing vapor nuclei, their patterns will be shaped by the structural history of evaporation. In our model the effective pinning of nanoparticles to vapor fronts is a consequence of the coupling between them and the solvent. This mechanism is similar in many respects to the Marangoni effect,<sup>26</sup> which experimentally is known to lead to cellular morphologies.<sup>28,80</sup> The other limit for which the evaporation rate is faster than the typical motion of the nanoparticles, fractal-like morphologies similar to diffusion limited aggregation<sup>81</sup> and fingering instabilities<sup>25</sup> form. As far as we know, the study of nanorods under such evaporation condition has not been explored experimentally. In this subsection we address this limit and the complexity introduced by the rotational motion of the nanorods.

In Figure 7 we plot a few representative simulation trajectories under heterogeneous evaporation conditions for a total coverage of 50%. The transition between homogeneous and heterogeneous

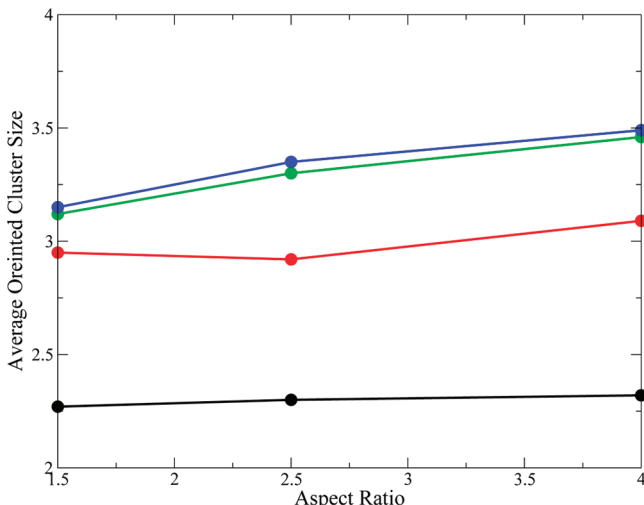


**Figure 8.** Average oriented cluster size as a function of the nanorods aspect ratio ( $1^{1/2}$  for  $6\xi \times 4\xi$ ,  $2^{1/2}$  for  $10\xi \times 4\xi$ , and 4 for  $16\xi \times 4\xi$ ) at different times (black  $t = 0$ , red  $t = 1/2$ , green  $t = 1$ , blue  $t = 2$  in units of  $\tau_l$ ) under heterogeneous evaporation conditions.

evaporation limits can be tuned by changing  $\mu$  or  $T$ .<sup>16,19</sup> For the results reported here, we have modified the temperature to values of  $T = 1/4$  in units of  $\epsilon_l$ . However, similar results were obtained when the chemical potential was varied instead. Upper, middle, and lower panel correspond to nanorods with an aspect ratio of  $1^{1/2}$  ( $6\xi \times 4\xi$ ),  $2^{1/2}$  ( $10\xi \times 4\xi$ ), and 4 ( $16\xi \times 4\xi$ ), respectively. We start from initial conditions that are similar to the initial conditions used for the homogeneous evaporation case (left frames), namely, nanorods fill random cells in the simulation box with random orientation and the remaining cells are filled with liquid.

The evolution of this state toward equilibrium is markedly different from the homogeneous evaporation case. Here, the solvent remains locally metastable on the surface and evaporation occurs by nucleation and growth of vapor bubbles. This is depicted in the middle snapshots shown in Figure 7 which were taken at intermediate times  $t = 1/2\tau_l$ . On the length scales shown only a single vapor bubble was formed for all three systems, in contrast to the case of homogeneous evaporation where many vapor bubbles were formed. Since vapor fluctuations are relatively rare, the time scale of evaporation  $\tau_l$  is significantly longer than in the homogeneous case.

The final morphologies shown in the right panels of Figure 7 were determinate by the structural history of evaporation, just like the case of heterogeneous drying-mediated assembly of spherical nanoparticles.<sup>16,18,20</sup> Following the evaporation the domain edges are effectively frozen, so that aggregation essentially halts when vapor nuclei meet to form network-like structures. Ordering within each domain occurs only in a narrow time window during the evaporation process itself. Before evaporation, the interparticle interactions are screened by the solvent such that particles do not stick and the nanorods have enough room to rotate. After evaporation is nearly complete the domains are frozen and the dense packing of nanorods along with the sticky conditions prevents any reorientation or rearrangement.

In the right panels of Figure 7 we plot the oriented cluster size distribution,  $P_C(n)$ , each frame corresponding to the trajectory shown to its left. The range of orientational order is typically longer under heterogeneous evaporation conditions for a given time (see also the average oriented cluster size under heterogeneous evaporation conditions shown in Figure 8

compared with the homogeneous case shown in Figure 6). However, since the range of orientational order increases slowly (algebraically) with time for the homogeneous case, eventually the range of orientational order under fluxional homogeneous evaporation conditions will exceed that of sticky heterogeneous dynamics, which reaches its maximal value at times  $t > 3\tau_l$ .

Similar to the homogeneous evaporation case, the range of orientational order increases with the increasing aspect ratio, as can be seen in Figure 8 where we plot the average oriented cluster size ( $\langle n \rangle = \sum_n n P_C(n)$ ) as a function of the aspect ratio at different times. As the system approaches the final metastable morphology, we find a linear correlation between the range of orientational order and the length of the nanorods for a given diameter. This is the case for both nanorod series studied in this work (diameters  $4\xi$  and  $2\xi$ ). However, the overall increase in the orientational range of order is quite small and extrapolations to nanorods with aspect ratios exceeding 20 will still result in a domain with relatively short-range order, regardless of whether the evaporation is homogeneous or heterogeneous, with the main limitations being the time scale associated with domain growth, evaporation dynamics, and mobility of the nanorods.

Before we move to discuss ways to achieve longer orientational order, we note that in both types of evaporation dynamics, when the nanorods density is relatively high, the evaporation leads to the formation of vapor holes that grow with time. When examining the assembly of the nanorods in the vicinity of the vapor holes, we find that the nanorods tend to align parallel to the circumference of the growing rims, which is consistent also with experimental observations.<sup>55–62</sup> At thermodynamic equilibrium, the alignment of the nanorods along the circumference of the rim will favor a perpendicular orientation, which minimizes the surface tension and the resulting capillary interactions.<sup>82–84</sup> The fact that the nanorods align parallel to the circumference of the rim is an indication that this structure is kinetically driven, either by the dynamics of the evaporation/nanorods diffusion, or by rearrangements of the nanorods into dense structures driven by solvation.

#### IV. Prealignment

The above examples of an initial random configuration indicate that long-range orientational alignment of the nanorods is difficult to achieve by drop casting. Thus, in order to align the nanorods along a predefined direction, there must be a mechanism that leads to such an alignment before the solvent evaporates, since the drying kinetic is too rapid to allow for the system to reach the thermodynamically stable aligned structure.<sup>71</sup> This can be achieved by several techniques such as applying magnetic and/or electric fields before and during the evaporation,<sup>63–69</sup> forcing the nanorods to align with the direction of the field. Alternatively, one can utilize capillary forces that are expected to be significant due to the spherical symmetry breaking of nanorods. One such example involves an experimental setup where the substrate is vertically aligned with respect to the reseeding liquid,<sup>15</sup> creating contact angle with the substrate at the air–liquid interface. In this geometry, as the density of nanorods increases due to the receding solvent front, the nanorods will experience strong directional capillary forces at the air–liquid–substrate contact line.<sup>85,86</sup>

The physical picture behind these two scenarios is quite different. The alignment forces in the former are preserved along the assembly process while for the latter they vanish as the system assembled into an ordered phase. Here, we wish to examine how the evaporating dynamics affect the alignment under prealigned initial conditions, where the forces for align-

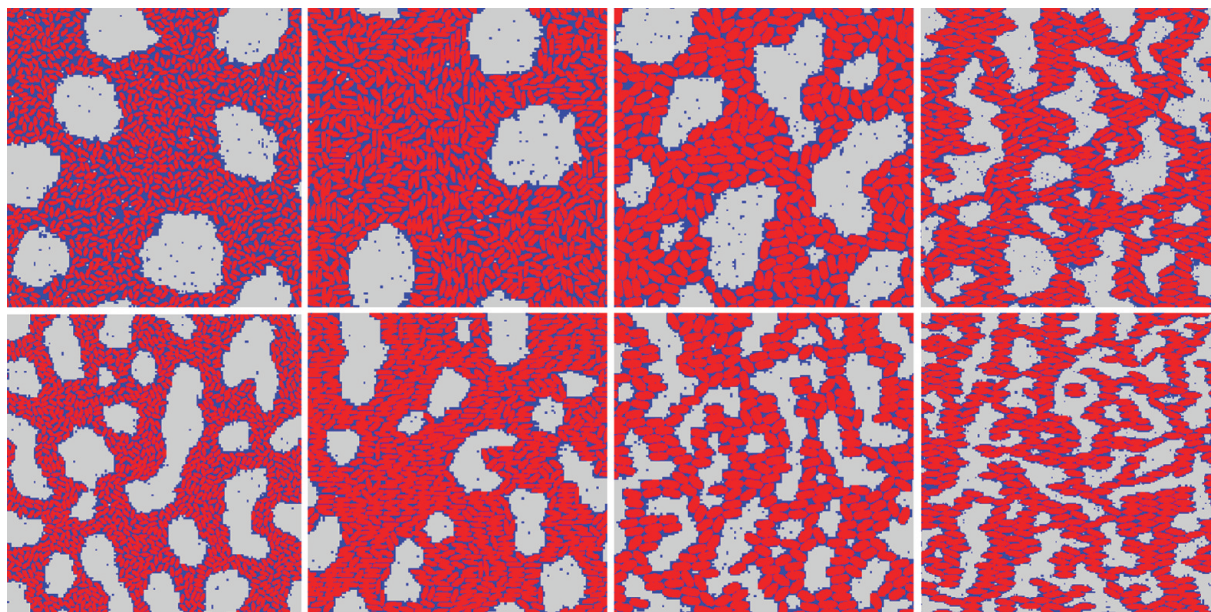


**Figure 9.** Representative morphologies of prealigned self-assembled nanorods under homogeneous evaporation conditions at long times. Upper and lower panels correspond to two different rates of evaporation ( $\tau_l = 10$  and 5, respectively). Panels from left to right correspond to nanorods of size  $6\xi \times 2\xi$ ,  $8\xi \times 2\xi$ ,  $10\xi \times 4\xi$ , and  $16\xi \times 4\xi$ .

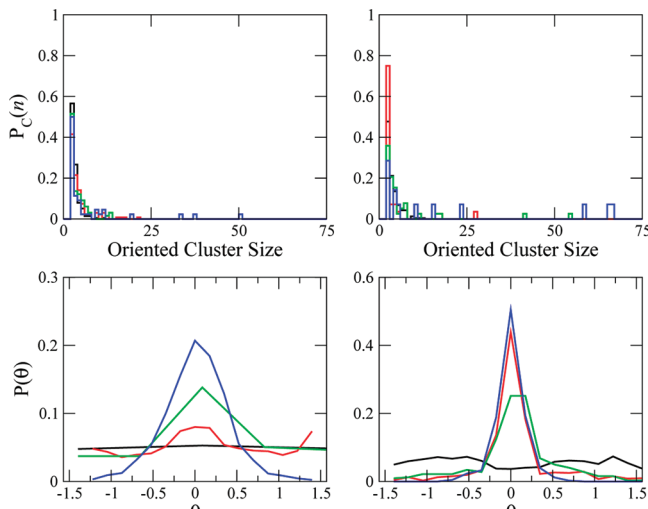


**Figure 10.** Upper panels: Oriented cluster size distribution  $P_C(n)$  for slow ( $\tau_l = 10$ , left panel) and fast ( $\tau_l = 5$ , right panel) evaporation for identical parameters as in Figure 9. The lower panels show the total orientational order for the same cases as in the upper panels. Black, red, green, and blue correspond to nanorods  $6\xi \times 2\xi$ ,  $8\xi \times 2\xi$ ,  $10\xi \times 4\xi$ , and  $16\xi \times 4\xi$ , respectively.

ment are turned off upon evaporation. The main issues to be addressed here are related to the interplay of drying kinetics and coarsening and their affect on the resulting morphologies when the nanorods start from an initial preferred orientation.

In Figure 9 we plot representative morphologies at long times for homogeneous evaporation of a prealigned system. Upper and lower panels corresponds to two different rates of evaporation. The different panels for each evaporation rate represent morphologies of nanorods with a different aspect ratio, as described in the figure caption. In Figure 10 we plot the corresponding oriented cluster size distribution  $P_C(n)$  (upper panels) and the overall angular distribution of the nanorods  $P(\theta)$  (lower panels) for the two evaporation rates.

Several features emerge from these results. If during the evaporation the nanorods have enough time to reorient, then the final morphology will resemble that of a random initial

configuration. This is clearly the case for the  $6\xi \times 2\xi$  nanorods, where the displayed morphologies at the slow and fast evaporation rates show random packing. The flat angular distribution shown in the lower panels of Figure 10 for this case quantitatively confirms this conjecture.

As the dimensions of the nanorods increase they become more and more sluggish (see Figures 4 and 5) and the final orientational order increases significantly. If the evaporation rate is slow, then the nanorods will still have enough time to “forget” their initial orientation. Comparing the total angular distributions in the lower panels of Figure 10 we find that  $P(\theta)$  becomes sharply peaked near the initial angular distribution as the evaporation rate increases and for nanorods with slower mobility. However, this is accompanied by smaller ordered domains with an increasing number of voids (see morphologies in Figure 9).

## V. Conclusions

We have developed a lattice gas model to treat the drying-mediated self-assembly of nanorods which accounts for the drying kinetics and the rotational and translational diffusion motion of the nanorods. Two distinct realizations of self-assembly experiments of nanorods were addressed: a random initial orientation corresponding to drop casting experiments and prealignment of the nanorods by capillary forces at the air–solvent interface. Analysis of the results was based on introducing the oriented cluster size distribution,  $P_C(n)$ , the overall angular distribution,  $P(\theta)$ , and the coarsening of nanorod domains.

We find that the mobility of nanorods reduces markedly with increasing diameter and with increasing aspect ratio. This leads to morphologies that are typically determined by the sluggish motion of the nanorods rather than by the rate of solvent fluctuations. Coarsening follows the typical scaling of  $t^\alpha$ , with an exponent that depends strongly on the aspect ratio and reduces from  $1/3$  to  $1/20$  when the aspect ratio increases to 4. For nanorods with an aspect ratio above  $5/2$ , the time scale accessible by simulations is too short to observe the crossover from the intermediate scaling to the long time behavior of  $t^{1/3}$ ,

providing an explanation as to why experimentally it is impossible to reach the thermodynamic stable ordered structure on time scale accessible by simulations or experiments.

These observations are consistent with the general picture that in drop casting experiments (random initial orientation), only local orientational order is observed. Our analysis shows that the range of order scales with the aspect ratio of the nanorods as long as time is scaled by the exponent  $\alpha$ , i.e., when order is measured at similar domain sizes.

Longer range order can be achieved if a mechanism for prealignment exists. We have discussed the dynamics of self-assembly under such conditions where the force acting on the nanorods before evaporation is turned off during the evaporation process itself. These conditions are typical of capillary forces that vanish when the solvent evaporates. Under such conditions we observe long-range order of nanorods as long as their motion is slow enough during the evaporation. Naturally, this cannot be achieved for nanorods with small aspect ratios, but for nanorods with aspect ratio above 4, this is a valuable route to achieve ordered morphologies.

**Acknowledgment.** We would like to thank Uri Banin, Haim Diamant, and Oded Millo for stimulating discussions and Uri Banin and Oded Millo for sharing their preliminary experimental results. C.G.S.-V. is a Clore Foundation Scholar. This work was supported in part by the EU under the program SA-NANO (grant no. STRP 013698) and by Israel Science Foundation (grant no. 283/07).

## References and Notes

- (1) Norris, D. J.; Bawendi, M. G.; Brus, L. E. Optical properties of semiconductors nanocrystals quantum dots. In *Molecular Electronics: A Chemistry for the 21st Century Monograph*; Jortner, J., Ratner, M. A., Eds.; Blackwell Science Inc.: Oxford, UK, 1997.
- (2) Alivisatos, A. P. *J. Phys. Chem.* **1996**, *100*, 13226.
- (3) El-Sayed, M. A. *Acc. Chem. Res.* **2004**, *37*, 326.
- (4) Murray, C. B.; Norris, D. J.; Bawendi, M. G. *J. Am. Chem. Soc.* **1993**, *115*, 8706.
- (5) Colvin, V. L.; Goldstein, A. N.; Alivisatos, A. P. *J. Am. Chem. Soc.* **1992**, *114*, 5221.
- (6) Ohara, P. C.; Leff, D. V.; Heath, J. R.; Gelbart, W. M. *Phys. Rev. Lett.* **1995**, *75*, 3466–3469.
- (7) Gelbart, W. M.; Sear, R. P.; Heath, J. R.; Chaney, S. *Faraday Discuss.* **1999**, *112*, 299–307.
- (8) Luedtke, W. D.; Landman, U. *J. Phys. Chem.* **1996**, *100*, 13323.
- (9) Korgel, B. A.; Fitzmaurice, D. *Phys. Rev. B* **1999**, *59*, 14191.
- (10) Rabani, E.; Egorov, S. A. *J. Chem. Phys.* **2001**, *115*, 3437.
- (11) Rabani, E.; Egorov, S. A. *Nano Lett.* **2002**, *2*, 69.
- (12) Rabani, E.; Egorov, S. A. *J. Phys. Chem. B* **2002**, *106*, 6771–6778.
- (13) Saunders, A. E.; Shah, P. S.; Park, E. J.; Lim, K. T.; Johnston, K. P.; Korgel, B. A. *J. Phys. Chem. B* **2004**, *108*, 15969–15975.
- (14) Lin, X. M.; Jaeger, H. M.; Sorensen, C. M.; Klabunde, K. J. *J. Phys. Chem. B* **2001**, *105*, 3353–3357.
- (15) Redl, F. X.; Cho, K. S.; Murray, C. B.; O'Brien, S. *Nature* **2003**, *423*, 968.
- (16) Rabani, E.; Reichman, D. R.; Geissler, P. L.; Brus, L. E. *Nature* **2003**, *426*, 271–274.
- (17) Sztrum, C. G.; Hod, O.; Rabani, E. *J. Phys. Chem. B* **2005**, *109*, 6741–6747.
- (18) Sztrum, C. G.; Rabani, E. *Adv. Mater.* **2006**, *18*, 565–571.
- (19) Yosef, G.; Rabani, E. *J. Phys. Chem. B* **2006**, *110*, 20965–20972.
- (20) Kletenik-Edelman, O.; Ploshnik, E.; Salant, A.; Shenhar, R.; Banin, U.; Rabani, E. *J. Phys. Chem. C* **2008**, *112*, 4498–4506.
- (21) Kletenik-Edelman, O.; Sztrum-Vartash, C. G.; Rabani, E. *J. Mater. Chem.* **2009**, *19*, 2872–2876.
- (22) Martin, C. P.; Blunt, M. O.; Moriarty, P. *Nano Lett.* **2004**, *4*, 2389–2392.
- (23) Martin, C. P.; Blunt, M. O.; Stannard, E. P.-V. A.; Moriarty, P.; Vancea, I.; Thiele, U. *Phys. Rev. Lett.* **2007**, *99*, 116103.
- (24) Blunt, M. O.; Martin, C. P.; Ahola-Tuomi, M.; Vaujour, E.; Sharp, P.; Nativo, P.; Brust, M.; Moriarty, P. *J. Nat. Nanotechnol.* **2006**, in press.
- (25) Pauliac-Vaujour, E.; Stannard, A.; Martin, C. P.; Blunt, M. O.; Notinger, I.; Moriarty, P. *J. Phys. Rev. Lett.* **2008**, *100*, 176102.
- (26) Maillard, M.; Motte, L.; Ngo, A. T.; Pileni, M. P. *J. Phys. Chem. B* **2000**, *104*, 11871–11877.
- (27) Maillard, M.; Motte, L.; Pileni, M. P. *Adv. Mater.* **2001**, *13*, 200–204.
- (28) Stowell, C.; Korgel, B. A. *Nano Lett.* **2001**, *1*, 595–600.
- (29) Ge, G.; Brus, L. E. *Nano Lett.* **2001**, *1*, 219–222.
- (30) Blunt, M. O.; Martin, C. P.; Ahola-Tuomi, M.; Pauliac-Vaujour, E.; Sharp, P.; Nativo, P.; Moriarty, M. B. P. *J. Nat. Nanotechnol.* **2007**, *2*, 167–170.
- (31) Peng, X. G.; Manna, L.; Yang, W. D.; Wickham, J.; Scher, E.; Kadavich, A.; Alivisatos, A. P. *Nature* **2000**, *404*, 59.
- (32) Puntes, V. F.; Krishnan, K. M.; Alivisatos, A. P. *Science* **2001**, *291*, 2115.
- (33) Cordente, N.; Respaud, M.; Senocq, F.; Casanove, M. J.; Amiens, C.; Chaudret, B. *Nano Lett.* **2001**, *1*, 565–568.
- (34) Murphy, C. J.; Jana, N. R. *Adv. Mater.* **2002**, *14*, 80–82.
- (35) Pileni, M. P. *Nat. Mater.* **2003**, *2*, 145–150.
- (36) Cozzoli, P. D.; Snoeck, E.; Garcia, M. A.; Giannini, C.; Guagliardi, A.; Cervellino, A.; Gozzo, F.; Hernando, A.; Achterhold, K.; Ciobanu, N.; Parak, F. G.; Cingolani, R.; Manna, L. *Nano Lett.* **2006**, *6*, 1966–1972.
- (37) Hoffmann, M.; Wagner, C. S.; Harnau, L.; Wittemann, A. *ACS Nano* **2009**, *3*, 3326.
- (38) Yin, Y. D.; Rioux, R. M.; Erdonmezand, C. K.; Hughes, S.; Somorjai, G. A.; Alivisatos, A. P. *Science* **2004**, *304*, 711–714.
- (39) Talapin, D. V.; Koeppe, R.; Gotzinger, S.; Kornowski, A.; Lupton, J. M.; Rogach, A. L.; Benson, O.; Feldmann, J.; Weller, H. *Nano Lett.* **2003**, *3*, 1677–1681.
- (40) Mokari, T.; Rothenberg, E.; Popov, I.; Costi, R.; Banin, U. *Science* **2004**, *304*, 1787–1790.
- (41) Mokari, T.; Sztrum, C. G.; Shaviv, E.; Rabani, E.; Banin, U. *Nat. Mater.* **2005**, *4*, 855–863.
- (42) Shevchenko, E. V.; Talapin, D. V.; O'Brien, S.; Murray, C. B. *J. Am. Chem. Soc.* **2005**, *127*, 8741–8747.
- (43) Kudera, S.; Carbone, L.; Casula, M. F.; Cingolani, R.; Falqui, A.; Snoeck, E.; Parak, W. J.; Manna, L. *Nano Lett.* **2005**, *5*, 445–449.
- (44) Hoffmann, M.; Lu, Y.; Schrinner, M.; Ballauff, M.; Harnau, L. *J. Phys. Chem. B* **2008**, *112*, 14843.
- (45) Lee, K. S.; El-Sayed, M. A. *J. Phys. Chem. B* **2006**, *110*, 19220–19225.
- (46) Fu, A. H.; Gu, W. W.; Boussert, B.; Koski, K.; Gerion, D.; Manna, L.; Le Gros, M.; Larabell, C. A.; Alivisatos, A. P. *Nano Lett.* **2007**, *7*, 179–182.
- (47) Kazes, M.; Lewis, D. Y.; Ebenstein, Y.; Mokari, T.; Banin, U. *Adv. Mater.* **2002**, *14*, 317–321.
- (48) Link, S.; El-Sayed, M. A. *J. Phys. Chem. B* **2002**, *92*, 6799–6803.
- (49) Cui, Y.; Banin, U.; Bjork, M. T.; Alivisatos, A. P. *Nano Lett.* **2005**, *5*, 1519–1523.
- (50) Hoffmann, M.; SiebenbÄErger, M.; Harnau, L.; Hund, M.; Hanske, C.; Lu, Y.; Wagner, C. S.; Drechsler, M.; Ballauff, M. *Soft Matter* **2010**, *6*, 1125–1128.
- (51) Huybh, W. U.; Dittmer, J. J.; Alivisatos, A. P. *Science* **2002**, *295*, 2425–2427.
- (52) Sun, B. Q.; Marx, E.; Greenham, N. C. *Nano Lett.* **2003**, *3*, 961–963.
- (53) Law, M.; Goldberger, J.; Yang, P. *Annu. Rev. Mater. Sci.* **2004**, *34*, 83.
- (54) Tang, Z.; Kotov, N. A. *Adv. Mater.* **2005**, *17*, 951–962.
- (55) Martin, B. R.; Dermody, D. J.; Reiss, B. D.; Fang, M. M.; Lyon, L. A.; Natan, M. J.; Mallouk, T. E. *Adv. Mater.* **1999**, *11*, 1021–1025.
- (56) Nikoobakh, B.; Wang, Z. L.; El-Sayed, M. A. *J. Phys. Chem. B* **2000**, *104*, 8635–8640.
- (57) Kim, F.; Kwan, S.; Akana, J.; Yang, P. D. *J. Am. Chem. Soc.* **2001**, *123*, 4360–4361.
- (58) Pacholski, C.; Kornowski, A.; Weller, H. *Angew. Chem.* **2002**, *41*, 1188.
- (59) Li, L. S.; Alivisatos, A. P. *Adv. Mater.* **2003**, *15*, 408.
- (60) Murphy, C. J.; San, T. K.; Gole, A. M.; Orendorff, C. J.; Gao, J. X.; Gou, L.; Hunyadi, S. E.; Li, T. J. *Phys. Chem. B* **2005**, *109*, 13857–13870.
- (61) Wu, J. J.; Lee, Y. L.; Chiang, H. H.; Wong, D. K. P. *J. Phys. Chem. B* **2006**, *110*, 18108–18111.
- (62) Ghezelbash, A.; Koo, B.; Korgel, B. A. *Nano Lett.* **2006**, *6*, 1832.
- (63) Harnack, O.; Pacholski, C.; Weller, H.; Yasuda, A.; Wessels, J. M. *Nano Lett.* **2003**, *3*, 1097–1101.
- (64) Ryan, K. M.; Mastrianni, A.; Stancil, K. A.; Liu, H. T.; Alivisatos, A. P. *Nano Lett.* **2006**, *6*, 1479–1482.
- (65) Gupta, S.; Zhang, Q. L.; Emrick, T.; Russell, T. P. *Nano Lett.* **2006**, *6*, 2066–2069.
- (66) Ahmed, S.; Ryan, K. M. *Nano Lett.* **2007**, *7*, 2480.
- (67) Carbone, L.; et al. *Nano Lett.* **2007**, *7*, 2942.
- (68) Nobile, C.; Carbone, L.; Fiore, A.; Cingolani, R.; Manna, L.; Krahe, R. *J. Phys.: Condens. Matter* **2009**, *21*, 264013.

- (69) Tanase, M.; Bauer, L. A.; Hultgren, A.; Silevitch, D. M.; Sun, L.; Reich, D. H.; Searson, P. C.; Meyer, G. *J. Nano Lett.* **2001**, *1*, 155–158.
- (70) Bolhuis, P. G.; Stroobants, A.; Frenkel, D.; Lekkerkerker, H. N. W. *J. Chem. Phys.* **1997**, *107*, 1551.
- (71) Bates, M. A.; Frenkel, D. *J. Chem. Phys.* **2000**, *112*, 10034–10041.
- (72) Savenko, S. V.; Dijkstra, M. *J. Chem. Phys.* **2006**, *124*, 234902.
- (73) TenWolde, P. R.; Sun, S. X.; Chandler, D. *Phys. Rev. E* **2001**, *65*, 011201.
- (74) TenWolde, P. R.; Chandler, D. *Proc. Natl. Acad. Sci. U.S.A.* **2002**, *99*, 6539–6543.
- (75) Brannigan, G.; Brown, F. L. H. *J. Chem. Phys.* **2004**, *120*, 1059–1071.
- (76) Bray, A. J. *Adv. Phys.* **2002**, *51*, 481–587.
- (77) van Bruggen, M. P. B.; Lekkerkerker, H. N. W.; Dhont, J. K. G. *Phys. Rev. E* **1997**, *56*, 4349–4403.
- (78) Tao, Y.-G.; den Otter, W. K.; Padding, J. T.; Dhont, J. K. G.; Briels, W. J. *J. Chem. Phys.* **2005**, *122*, 244903–1–10.
- (79) Ratke, L.; Voorhees, P. W. *Growth and Coarsening: Ostwald Ripening in Material Processing*; Springer: Berlin, Germany, 2002.
- (80) Ge, G.; Brus, L. E. *J. Phys. Chem B* **2000**, *104*, 9573–9575.
- (81) Witten, T. A.; Sander, L. M. *Phys. Rev. Lett.* **1981**, *47*, 1400–1403.
- (82) Kralchevsky, P. A.; Paunov, V. N.; Ivanov, I. B.; Nagayama, K. *J. Colloid Interface Sci.* **1992**, *151*, 79–94.
- (83) Kralchevsky, P. A.; Nagayama, K. *Langmuir* **1994**, *10*, 23–36.
- (84) Kralchevsky, P. A.; Nagayama, K. *Particles at Fluid Interfaces and Membranes: Attachment of Colloid Particles and Proteins to Interfaces and Formation of Two-Dimensional Arrays*; Elsevier: Amsterdam, The Netherlands, 2001.
- (85) Steine, D.; Azulay, D.; Aharoni, A.; Salant, A.; Banin, U.; Millo, O. *Phys. Rev. B* **2009**, *80*, 195308.
- (86) Banin, U.; Millo, O. Private communication.

JP1015559